

Tensile yield strength of a single bulk Al_{0.3}CoCrFeNi high entropy alloy can be tuned from 160 MPa to 1800 MPa

Bharat Gwalani^{1,2}, Stephane Gorsse^{3,4}, Deep Choudhuri^{1,2}, Y. Zheng⁵, Rajiv S. Mishra^{1,2}, and Rajarshi Banerjee^{1,2*}

¹ Advanced Materials and Manufacturing Processes Institute, University of North Texas
Denton, TX-76207, USA

² Department of Materials Science and Engineering, University of North Texas
Denton, TX-76207, USA

³ CNRS, ICMCB, UMR 5026, 33600 Pessac, France

⁴ Bordeaux INP, ENSCBP, 33600 Pessac, France

⁵ Department of Materials Science and Engineering, The Ohio State University, Columbus, OH 4310,
USA

* Corresponding author: Rajarshi.Banerjee@unt.edu

Abstract

While there have been multiple recent reports in the literature of exceptional combinations of yield strength and ductility in high entropy alloys, there have been no reports discussing the extraordinary tunability of the mechanical properties in the same alloy in these systems. This paper shows that the tensile yield-strength of a single Al_{0.3}CoCrFeNi high entropy alloy (or complex-concentrated alloy), can be enhanced from 160 MPa to over 1800 MPa (1.8 GPa), a 1025% increase, via microstructural engineering enabled by thermo-mechanical processing of the bulk alloy. Such strength variations for the same composition are unprecedented in any other class of alloys.

Keywords: High entropy alloys, characterization, mechanical properties, complex concentrated alloys, clusters

The investigation of high entropy alloys (HEAs) began with the pioneering work of Cantor [1] and Yeh [2] in 2004. They simultaneously showed that a fully austenitic microstructure, consisting of single face-centered cubic (fcc) phase, was obtained in equiatomic mixtures of multiple elements, having different crystal structures. These pioneering efforts created the groundwork for a new concept in alloy design by advocating that severe lattice distortion in concentrated disordered solid solutions can promote high strength and retain ductility, without the deleterious effect of embrittling intermetallic or other compound phases in structural alloys. Subsequently, a substantial effort has been directed towards finding new equiatomic combinations of elements to promote the formation of *fcc*, *bcc* or *hcp* single-phase-disordered solid solutions, presumably stabilized by the configurational entropy of mixing. However, despite the exceptional fracture toughness properties exhibited by the CoCrFeNiMn alloy [3], also referred to as Cantor alloy, the ability of the HEA concept to revolutionize alloy design, and lead to exceptional mechanical performance, seems limited since it involves only one principal strengthening mechanism, i.e. solid solution strengthening.

Recently, the HEA community returned to the basics of physical metallurgy, i.e. microstructural engineering by altering alloy composition (chemistry) and thermomechanical processing (simultaneous application of temperature and stresses) to enhance the balance of mechanical properties in HEAs [4-7]. The result was the adoption of two well-known microstructure templates, found in dual-phase (fcc austenite + body centered tetragonal or hexagonal martensite) TRIP steels [8], and age-hardenable Ni alloys (fcc austenite + ordered intermetallic L₁₂ or γ' precipitates) [9], to these new alloys. These studies elucidated the applicability and efficacy of traditional metallurgical approaches for the development of the second generation of multi-phase HEAs, also referred to as complex concentrated alloys (CCAs) [4-6] or multi-principal element alloys (MPEAs), with often unequal proportion of principal elements and microstructures comprising multiple phases. However, the composition of these “HEAs”, e.g. Fe₅₀Mn₃₀Co₁₀Cr₁₀ HEA [8] become comparable to high-Mn steels [10], and somewhat deviate from the notion of HEAs, because their compositions shift towards the edges of the composition space where conventional alloys already lie. We emphasize that the HEA design concept mandates searching for alloy compositions that are located in the interior regions of multi-component phase diagrams [6]. In the present study, we highlight a different approach that takes advantage of the compositional complexity of these concentrated alloys. This

complexity leads to an exceptionally vast array of possible microstructures and phases that can be generated, in a selected phase field of operation, for the *same alloy composition*. This distinguishing feature of HEAs, which has not been explored yet, opens up the avenue for *materials with properties that can be tuned over a broad range of values without changing the composition*.

To explore the concept of highly tunable HEA, we have selected the $\text{Al}_{0.3}\text{CoCrFeNi}$ composition, as a candidate alloy, because it encompasses a remarkably large number of phase fields as a function of temperature. For example, with decreasing temperature, this HEA composition traverses from a single *fcc* phase field to *fcc+B2* (ordered bcc), *fcc+B2+sigma* (σ), *B2+L1₂+sigma*, and finally at lower temperatures, a *B2+L1₂+bcc+sigma* phase field (Fig. 1). Such a unique richness of the complex multi-phase landscape offers the designer more options to tailor the phase combinations and the microstructural length scales, with one or more intermetallic/ordered phases, employing different thermo-mechanical treatments. Accordingly, such a vast array of multi-phase microstructures offers a unique opportunity to tune the properties over a staggeringly wide range in the same alloy.

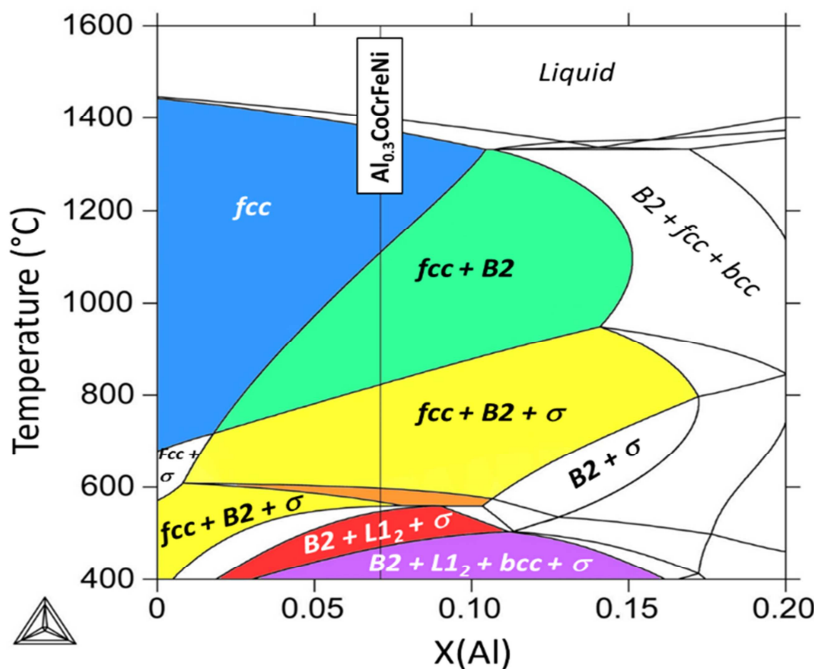


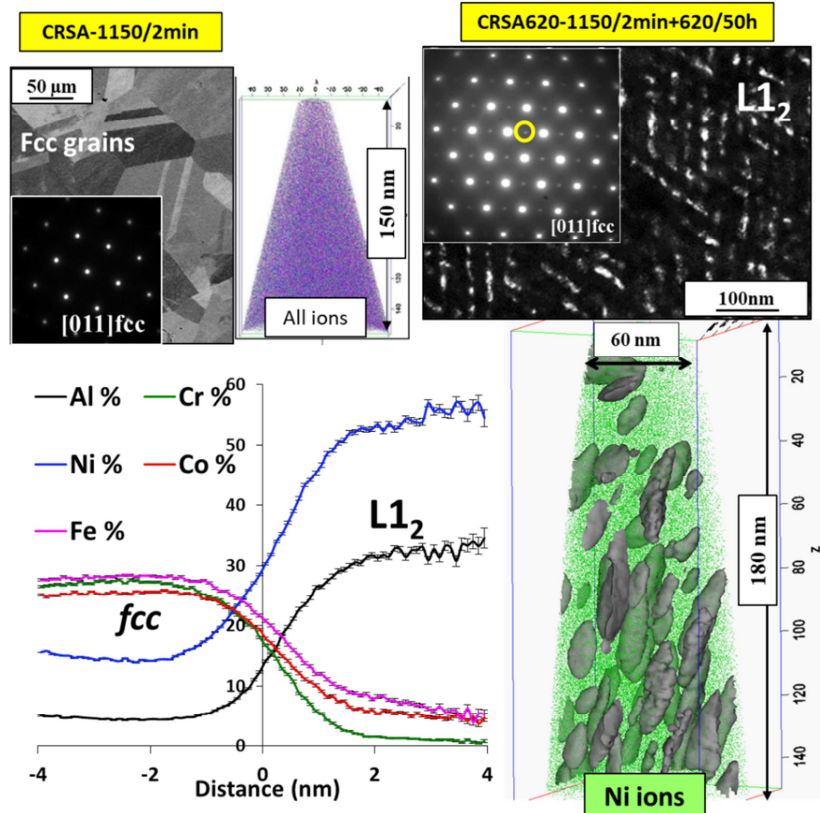
Fig. 1. Isopleth for $Al_xCoCrFeNi$. This section of the Al-Co-Cr-Fe-Ni quinary system was calculated using the TCHEA2 thermodynamic description from ThermoCalc. It shows possible phases as a function of Al content and temperature.

The $Al_{0.3}CoCrFeNi$ HEA was synthetized via arc melting using pure metals, solutionized at 1150°C for 10h and cold-rolled to 90% thickness reduction. Subsequently, sections of the cold-rolled alloy were subjected to four different thermal treatments: (a) recrystallization at 1150°C (hereafter referred to as CRSA), and (b) annealing at 620°C for 50h to promote second phase precipitation (hereafter referred to as CRSA620-50), or direct annealing of the heavily deformed cold-rolled specimens at (c) 620°C for 50h (hereafter referred to as CR620-50) or (d) 550°C for 24h (hereafter referred to as CR550-24) and 50h (hereafter CR550-50) to promote concurrent recrystallization and second phase precipitation.

Microstructural characterization was performed using scanning electron microscopy (SEM) (FEI Nova-NanoSEM 230TM). The tensile tests were carried out by setting the initial strain rate at 10^{-3} s⁻¹, with respect to change in length. The tensile test specimens (gauge length ~ 3 mm, width ~ 1 mm and thickness ~ 0.5–1 mm) were machined using electric discharge machine (EDM). At least five independent tests were carried out to obtain tensile elongation and strength data. Conventional transmission electron microscopy (TEM) studies were carried out on a FEI Tecnai G2 TF20TM operating at 200 kV. Precipitate characterization was done using conventional and high angle annular dark field-scanning TEM (HAADF-STEM) modes. To measure the composition, energy dispersive spectroscopy (Super-X system) equipped on an FEI-TITAN G2 TEM microscope was used in the HAADF STEM mode operating at 300 kV and the results were analyzed with FEI's ES vision software version 6. TEM foils were prepared by an FEI Nova Nanolab 200 dual-beam focused ion beam (FIB) instrument using a Ga ion beam for milling. Standard lift-out techniques were used for Atom Probe Tomography (APT) sample preparation in the FIB before mounting the small sections of the samples on suitable holders for analysis. APT experiments were conducted on a CAMECA local electrode atom probe 3000X HR instrument.

A single *fcc* phase with uniform elemental distribution was obtained after recrystallization at 1150°C (**Fig. 2A**, CRSA condition). Subsequent annealing at 620°C for 50 hrs (CRSA620 condition), lead to a homogeneous distribution of ordered (Al,Ni)-rich L1₂ precipitates

throughout the *fcc* matrix (**Fig. 2B & C**). When concurrent recrystallization and precipitation occur by direct annealing the samples at 620°C after cold-rolling (CR620 condition), the alloy has a triplex, or three-phase microstructure comprising of *fcc* phase, (Al,Ni)-rich B2 precipitates, and Cr-rich σ precipitates (**Fig. 3A**). Finally, when the same alloy is annealed at 550°C directly after cold-rolling (CR550-24 condition), the microstructure revealed two new additional features as compared to the CR620 condition: fine scale B2/*bcc* two-phase precipitates, and even finer, nanometer-scale (Al,Ni)-rich clusters uniformly distributed within the *fcc* matrix (**Fig. 3B**). The formation of conjoint B2/*bcc* on annealing at low temperature in a $\text{Al}_x\text{CoCrFeNi}$ alloy system is also shown by Rao et. al [11]. The CR550-50 condition exhibited a similar microstructure as the CR550-24 sample. Interestingly, in all cases, the *fcc* matrix retained a high entropy like



composition i.e. $\text{Al}_{0.1}\text{CoCrFeNi}_{0.5}$ even after second (or third) phase precipitation (for example refer to **Fig. 2C**). Notwithstanding, these four types of microstructures, obtained for the same alloy composition, elucidate the rationale of this work; i.e the widely varying combination of phases and microstructural length scales that can be achieved for the same HEA composition.

Fig. 2. Variety of the microstructures of the $\text{Al}_{0.3}\text{CoCrFeNi}$ CCA for different processing conditions. SEM image showing the recrystallized grains from sample **CRSA** (A) along with the $[011]_{\text{fcc}}$ zone axis diffraction pattern, and atom probe tomography (APT) showing the 3D reconstructions of Al, Co, Cr, Fe and Ni ions. The results show the presence of a single solid solution fcc phase.

Dark field transmission electron microscope (DFTEM) image along with the corresponding $[011]$ zone axis diffraction pattern, and atom probe tomography (APT) showing the 3D reconstructions of Al, Co, Cr, Fe and Ni ions and 15 at.% Al iso-concentration surface outlining L1_2 precipitates in a typical APT tip from sample **CRSA620** (B). The compositional profile using a proximity histogram across the fcc- L1_2 interface shows the compositional partitioning of various elements.

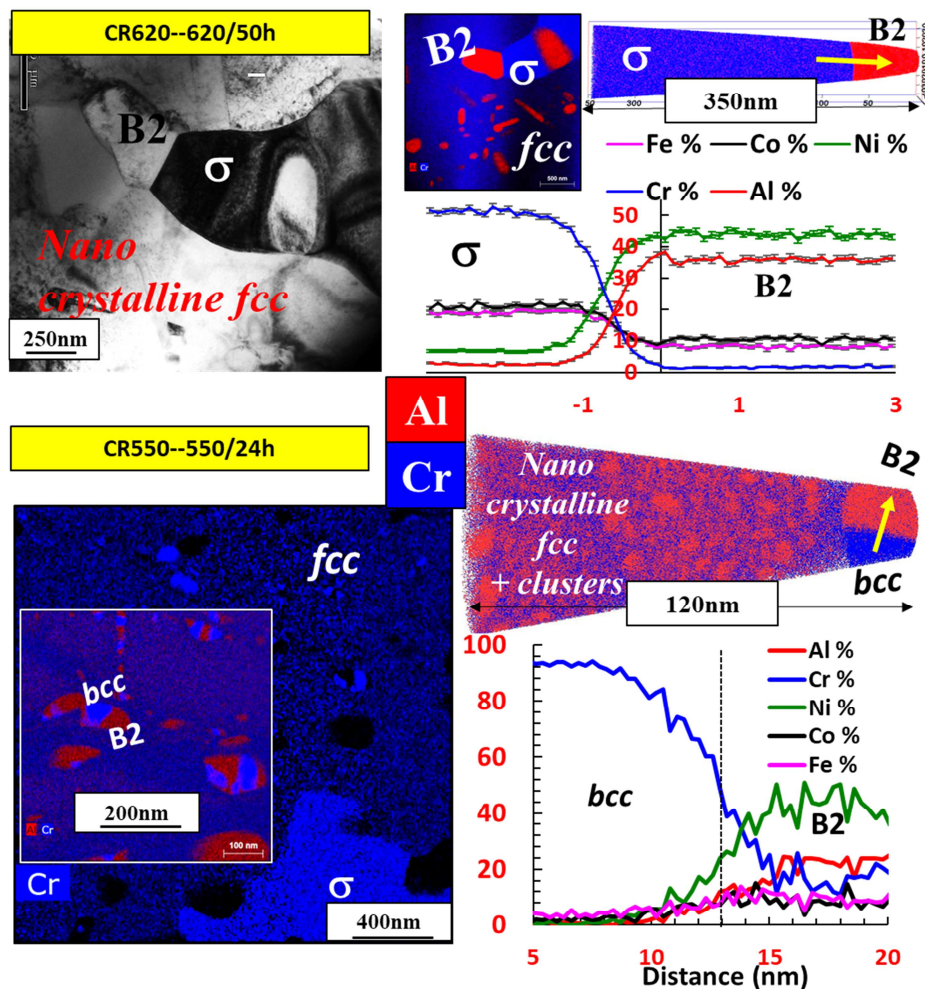


Fig. 3. Variety of the microstructures of the $\text{Al}_{0.3}\text{CoCrFeNi}$ CCA for four processing conditions. BFTEM and STEM-EDS maps of Al and Cr, and 3D reconstructions of atoms/ions Al and Cr, as marked, in a typical APT tip from samples **CR620** (C) and **CR550** (D). The

compositional profile using one-dimensional cylinder across the various interfaces as marked in the figure shows the compositional partitioning of various elements.

Fig. 4 (A) shows the room temperature engineering stress-strain curves for these five conditions. The corresponding true stress-strain curves for the same conditions are shown in **Fig. S1 (A)**. The single *fcc* microstructure HEA (CRSA) exhibits an ultimate tensile strength (UTS) of ~400 MPa and a ductility (elongation to failure under tension) of ~65 %. The introduction of precipitation hardening (L_{12} precipitation) in this alloy (CRSA620-50 condition), resulted in an UTS increase by 40 %, reaching 850 MPa, while maintaining an excellent ductility of ~45 %. The triplex CCA (CR620-50 condition) exhibits a remarkable strength-tensile ductility compromise of 1050 MPa and ~35 %. The CR550-24 condition with the most complex multi-scale microstructure, exhibits an even higher UTS (1850 MPa), an exceptionally high value for an *fcc*-based “austenitic-like” alloy, but a lower tensile ductility (~5%). Similarly, the CR550-50 condition exhibits a very high UTS value of 1650 MPa and a ductility ~7%. The main difference between the CR550-24 and CR550-50 conditions is that while there is virtually no strain hardenability remaining in case of the former condition, the latter condition exhibits some limited strain hardenability.

Fig. 4 (A) (inset) reveals a large range in the mechanical properties of $Al_{0.3}CoCrFeNi$ as a function of processing conditions (or microstructures; see Figures 2 and 3) and a notable difference in the strain hardening responses. In the single-phase HEA, the strain hardening rapidly drops and then remains nearly constant at a rate of 1000-1300 MPa before decreasing again. This behavior during plastic deformation is similar to that of low-stacking fault energy alloys such as CoCrFeMnNi-based HEA [12], $Al_{0.1}CoCrFeNi$ [14] and TWIP steels [15], which harden at room temperature at a rate of 1000-1500 MPa, 740 MPa, and 800-1200 MPa, respectively. The strain hardening of the multi-phase CCAs, i.e. CRSA620 and CR620, is initially much higher than the single-phase HEA, i.e between 1500-2000MPa, (see **inset Fig. 4 and Fig S1 (B)**). These observations indicated that differences in strain hardening result from the formation of secondary-phases (e.g. L_{12} or $B2/\sigma$) and the corresponding change in the *fcc* matrix composition i.e. $Al_{0.15}CoCrFeNi_{0.5}$ and $Al_{0.1}CoCrFeNi_{0.5}$ of CRSA620 and CR620 conditions respectively. The consequent reduction in both Ni and Al, both of which typically have high SFEs (146 mJ/m² for Al (lattice constant of 0.405 nm), 120.3 mJ/m² for Ni (lattice constant of

0.352 nm)) [16], is expected to reduce the SFE in the *fcc* matrix of the HEA. Furthermore, such reduction in SFE is typically associated with enhanced twinning in steels [17]. Similar observation was also noted in our studies, where the fcc matrix of CR620 had coarser deformation twins as compared to the simple phase in CRSA (compare supplementary **Figures S2 and S3**). It may be emphasized that twining is often associated with high strain-hardenability and good ductility [17, 18], and both properties are readily evident in the CR620 (containing fcc-B2- σ) and CRSA620 (*fcc*-L1₂) conditions. Therefore, it is likely that deformation twins, in the two conditions, will interact with mobile dislocations during quasi-static straining, and enhance strain-hardenability by increasing dislocation storage per the Kock-Mecking criterion [19].

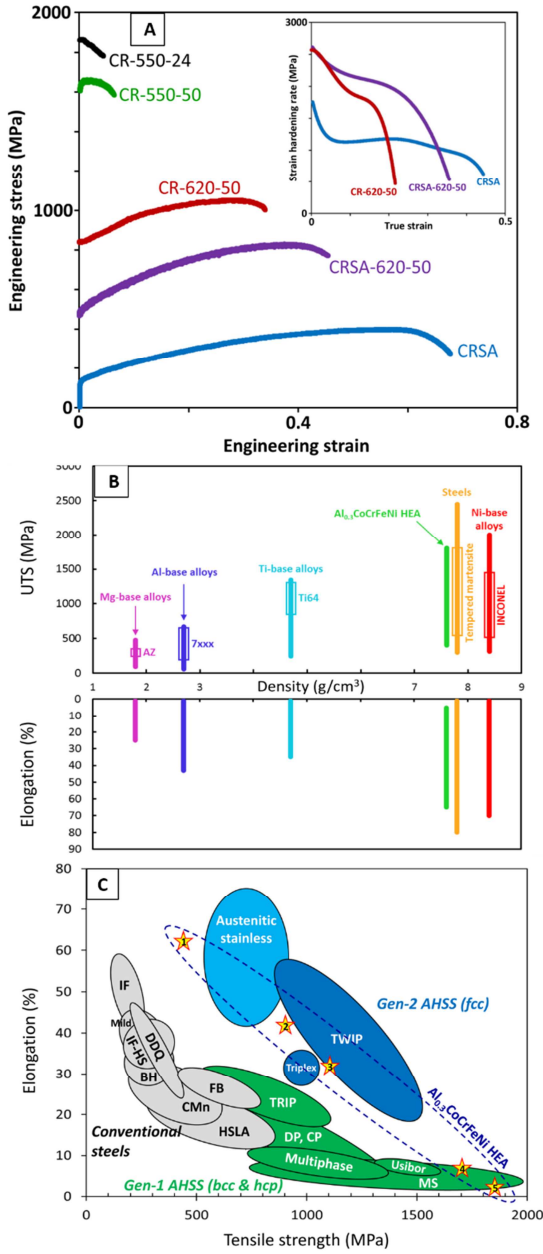


Fig. 4. (A) Mechanical behavior at room temperature of the $\text{Al}_{0.3}\text{CoCrFeNi}$ CCA. Engineering stress-strain and strain hardening vs true strain curves (inset).

(B) Ranges of ultimate tensile strength and ductility achieved by $\text{Al}_{0.3}\text{CoCrFeNi}$ in comparison with the main classes of structural alloys including present generation automotive and aerospace engineering alloys.

(C) Materials property space for room temperature elongation vs tensile strength of steels and $\text{Al}_{0.3}\text{CoCrFeNi}$ CCA. This strength-ductility diagram shows the range of properties achieved by $\text{Al}_{0.3}\text{CoCrFeNi}$ CCA (represented by stars 1-4) in comparison with all steel grades which are classified in three groups in addition to stainless steels. Conventional steels include low-

strength steels, e.g. interstitial-free (IF)) and mild steels, and conventional high strength steels, e.g. bake hardenable, high-strength low alloy (HSLA) and ferritic-bainitic (FB) steels. The first generation of advanced high-strength steels (AHSS) consist of ferritic matrix containing a hard martensite phase, i.e. dual phase (DP), retained austenite, i.e. transformation induced plasticity (TRIP), or small amounts of austenite and pearlite in ferrite/bainite matrix, i.e. complex phase (CP), or martensitic matrix containing small amount of ferrite/bainite, i.e. martensitic (MS) steels. The second generation of AHSS is austenitic steels with twinning induced plasticity (TWIP) and triplex steels.

A simplistic strength model can be employed to estimate the strengthening contribution of different microstructural features.

The yield strength can be approximated using the following equation:

$$\sigma_y = \sigma_{HP} + \Delta \sigma_{dis} + \Delta \sigma_{ppt} \text{ (MPa)} \quad (1)$$

where σ_{HP} is the combined effect of strengthening contributions from lattice friction, solid solution, and grain size (Hall-Petch). $\Delta \sigma_{dis}$ and $\Delta \sigma_{ppt}$ are the additional strengthening contributions from dislocations and precipitates, respectively.

In the CR-620 condition, the composition of the fcc matrix is $Al_{0.1}CoCrFeNi_{0.5}$ (from APT analysis). Kumar et al. [21] developed a Hall-Petch type equation for the yield strength as a function of grain size ($\sigma_{HP} = 174 + \frac{371}{\sqrt{d}}$ MPa) for the single fcc solid solution phase $Al_{0.1}CoCrFeNi$ HEA. The CR-620 condition in the present study, exhibits an average grain size $\sim 1.2 \mu m$ (refer **Figure S4**), and consequently the Hall-Petch strengthening can be estimated to be ~ 512 MPa (based on [21]). Hence, it can be assumed that 850 MPa (YS) - 512 MPa (HP) = 338 MPa is the strengthening contribution due to the hard intermetallic B2/ sigma precipitates and dislocations.

Likewise, in the CR-550-24 condition, (YS=1850 MPa) average grain size is ~ 0.4 micron (refer to **Figure S4**). The Hall-Petch strengthening contribution can be estimated to be ~ 760 MPa. Based on simple image analysis (using the ImageJ software) the approximate fraction of B2+sigma phase in CR-620 and CR-550 are 19% and 15% and therefore the strengthening contribution can be assumed similar and ~ 338 MPa. Therefore, the additional strength enhancement in case of the CR-550-24 condition, can be attributed to the presence of nano-clusters or precipitates, and this enhancement can be estimated to be 1850 MPa (YS) – 760 MPa (HP) – 338 MPa (B2/Sigma/dislocations) = 752 MPa.

The strength enhancement due to nano-precipitates can be estimated by using a simple Orowan strengthening model, based on the shearing of these nano-precipitates by dislocations. It can be described by the equation below:

$$\sigma_{\text{orowan}} = \frac{G * b}{\lambda} \quad (2)$$

$$(3) \quad \lambda = \frac{4(1-f)r}{3f}$$

Where λ is average planar center-to-center distance between nano-precipitates, G is the shear modulus of the matrix, b is the Burgers vector (assumed to be 80 GPa and 0.255nm for CoCrFeNiMn respectively [22]), r, the radius of the nano-precipitates (2 nm), and f, the volume fraction of precipitates (10 % by vol.), assessed from the APT results. Based on equations (2) and (3), the Orowan strengthening can be estimated to be ~850 MPa, which compares reasonably well with the experimentally observed strengthening value of 752 MPa. Therefore, the extraordinarily high value of yield strength ~1850 MPa in case of the CR-550 condition is a result of the contributions from hierarchical features ranging from thousands of nanometers (grain boundaries) to hundreds of nanometers (B2/sigma) to few nanometers (clusters).

DongYue et al. showed the impact toughness of single phase Al_{0.3}CoCrFeNi was much superior to steels [20]. An estimation of the toughness for the different types of microstructures in the same HEA (Al_{0.3}CoCrFeNi) has been carried out by calculating the area under the stress-strain curve (refer **Figure S5**). Quite remarkably, after second phase precipitation, the toughness of the CRSA620 and CR620 alloys increased, as compared to the CRSA condition.

The multiple combinations of hierarchical multi-phase microstructures, *observed for a single HEA composition, provide the largest range of strength-ductility combinations observed in any engineering class of structural metallic materials in their bulk form (Fig. 4(B))*, which is only attainable by accounting several grades of advanced high-strength-steels (AHSS) as shown by the strength-ductility diagram for steels (**Fig. 4(C)**). The vast range of mechanical properties achieved by the single Al_{0.3}CoCrFeNi HEA has been further put into perspective by plotting the strength-ductility values for the five conditions on a plot encompassing all presently known steels, as illustrated in **Fig. 4C**.

Remarkably, the range of mechanical properties exhibited by the single $\text{Al}_{0.3}\text{CoCrFeNi}$ HEA encompasses three different groups of steels. The first group belongs to ductile austenitic stainless steels with which the present HEA shares several common major elements (i.e. Fe, Cr, Ni) and the same single-phase austenitic, i.e. face-centered cubic (*fcc*), microstructure. The second group combines high strength and high ductility due to intense work hardening. This includes Twinning-Induced Plasticity (TWIP) and Triplex (e.g Fe-Mn-C-Al) grades of steels for which strain hardening mechanisms are controlled by the stacking fault energy (SFE). These steels have a high manganese content that causes the stabilization of the austenite and adjusts the SFE at the appropriate value to activate deformation twinning, resulting in multi-stage strain hardening [8, 10-12]. The third group, e.g. Martensitic steels (MS), have higher strength and lower ductility achieved by a martensitic matrix containing small amounts of ferrite and/or bainite [13].

The exceptionally large variety of mechanical behaviors and microstructures observed in the single $\text{Al}_{0.3}\text{CoCrFeNi}$ HEA emphasizes one of the unique features arising from the concept of HEAs as complex concentrated alloys.

The tunability of the mechanical response exhibited by the $\text{Al}_{0.3}\text{CoCrFeNi}$ HEA has the potential to solve two major problems. Today structural applications employ several materials to meet the requirements that often conflict. For example, in the automotive industry this involves the welding and bonding of different grades of steels, which is challenging because they differ in chemical composition. The exceptionally high tunability at constant composition of $\text{Al}_{0.3}\text{CoCrFeNi}$ HEA avoids this problem while meeting various functional requirements. The second concerns the development of architected materials. This concept has been depicted in the seminal work of O. Bouaziz et al. [23-25] as an innovative strategy for structural materials development to provide otherwise conflicting properties. The idea is to tailor the spatial distribution of the microstructure in a given topology and geometry in order to vary the mechanical properties in the overall component. Basu et al. emphasized on role of interfaces between crystallographically dissimilar phases on the size-dependent plasticity in multiphase HEAs [26-28]. Such a strategy has been underexploited because it relies on the fabrication of compositionally graded materials, which often require new processing methods. This obstacle could be overcome by the present HEA ($\text{Al}_{0.3}\text{CoCrFeNi}$) which features a unique range of

microstructures attainable using thermo-mechanical processing without changing the alloy composition.

Supplementary Materials

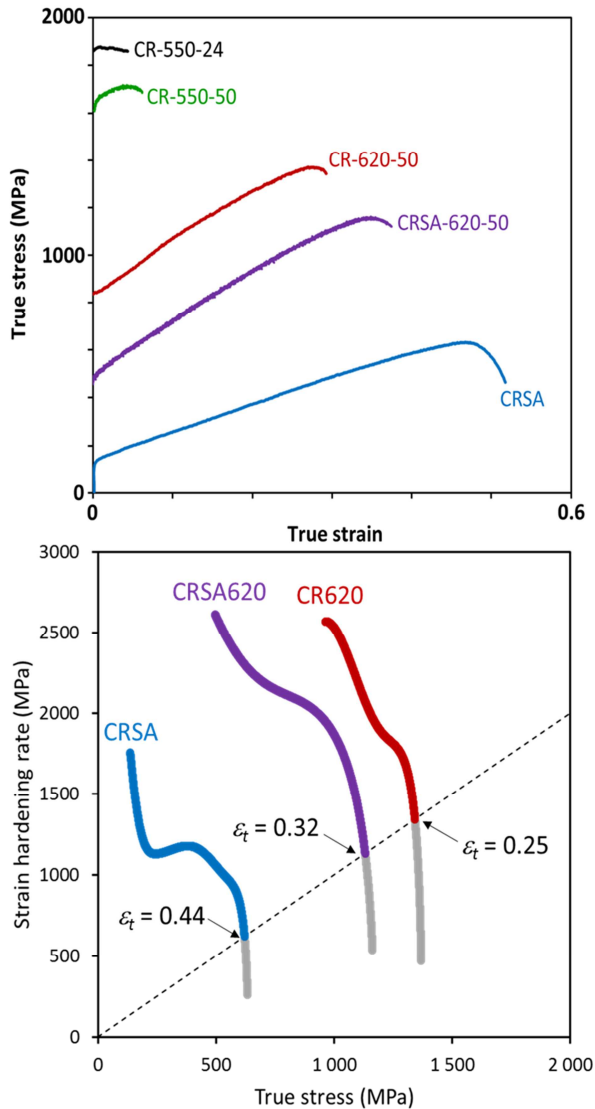


Figure S1. (A) Mechanical behavior at room temperature of the $\text{Al}_{0.3}\text{CoCrFeNi}$ CCA. True stress-strain curves (B) Consideré's criterion for onset necking. Work hardening rate (derivative of the true stress-strain curves) as a function of the true stress. Geometric instability is predicted to occur when the work hardening rate equals the true stress.

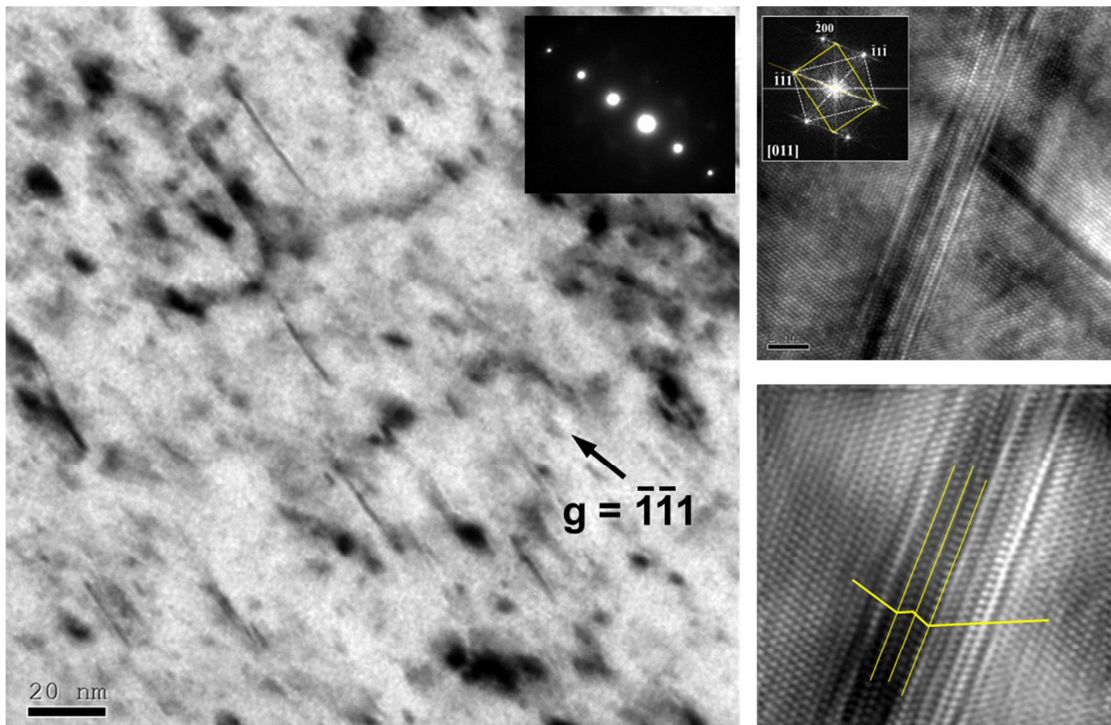


Figure S2. Deformation features in the single-phase $\text{Al}_{0.3}\text{CoCrFeNi}$ HEA (CRSA). High-resolution phase-contrast image of one of the fine scale features are shown in the image on left reveals them to be nano-scale twins approximately 1nm thick (see image on the right side). The TEM of single-phase microstructure indicate that deformation occurs via combination of extensive dislocation plasticity and nano-twinning.

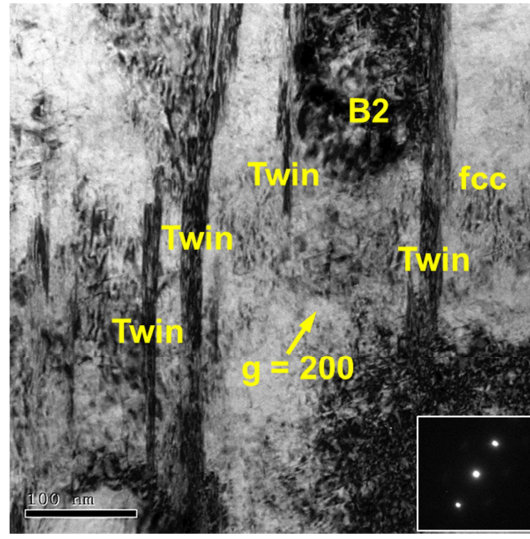


Figure S3. Deformation features in the triplex $\text{Al}_{0.3}\text{CoCrFeNi}$ CCA (CR620). BFTEM recorded with $g = 200$ depicts the probable origin of the deformation twins, i.e from B2-fcc triple junction and a high angle grain boundary (HAGB). The imaging condition also revealed dense

dislocations, e.g. see lower right-hand corner. These results indicate that triplex microstructure experience substantial twining compared to the single-phase fcc microstructure.

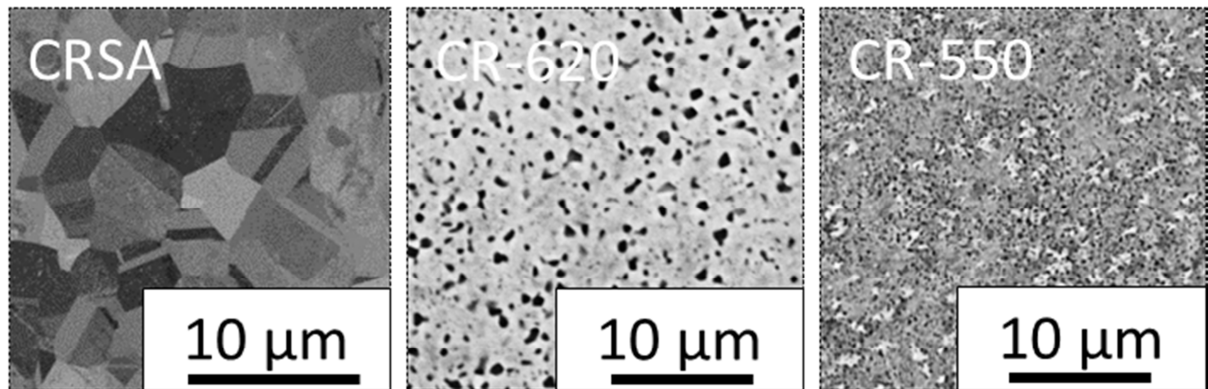


Figure S4. SEM BSED images from the different heat treatment conditions showing the drastic change in the grain sizes. The grain size in CRSA condition is 23 μm , CR-620 is 1.2 μm and in CR-550 condition is 0.4 μm .

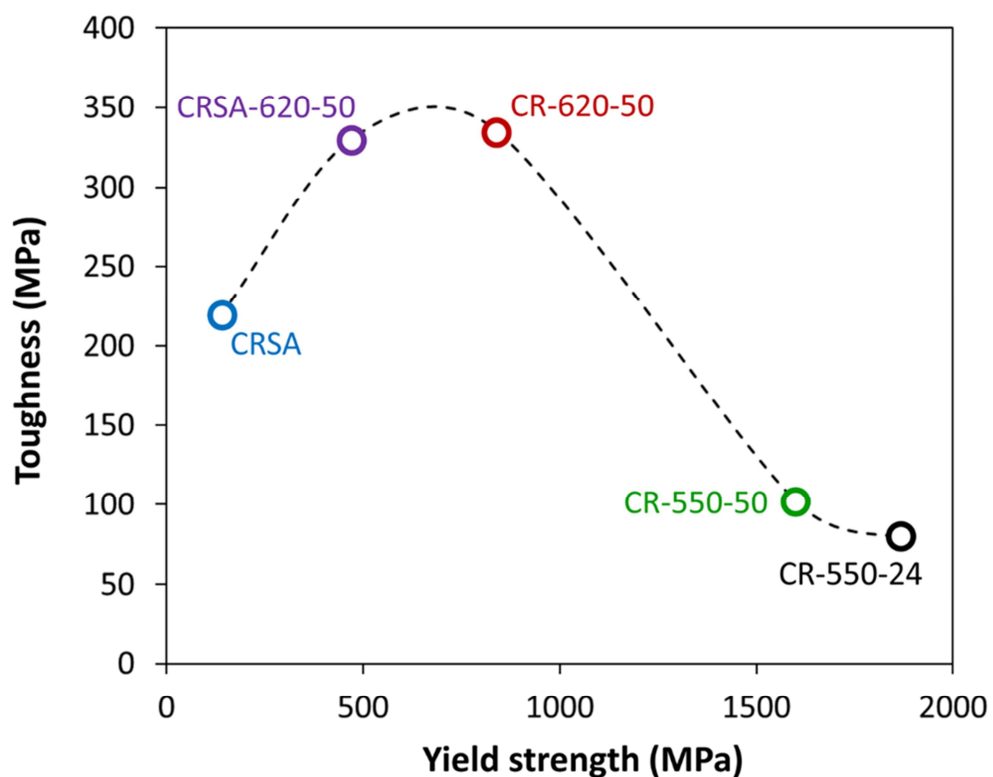


Figure S5. Variation of toughness (approximation by calculating the area under stress-strain curve) with microstructural changes in the $\text{Al}_{0.3}\text{CoCrFeNi}$ CCA

Acknowledgement

The work was performed under a cooperative agreement between the Army Research Laboratory and the University of North Texas (W911NF-16-2-0189). The authors also acknowledge the Materials Research Facility (MRF) at the University of North Texas for use of microscopy and atom probe tomography facilities, and the Center for Electron Microscopy and Analysis (CEMAS) at the Ohio State University, for microscopy facilities.

Figure captions:

Figure 1. Isopleth for $\text{Al}_x\text{CoCrFeNi}$. This section of the Al-Co-Cr-Fe-Ni quinary system was calculated using the TCHEA2 thermodynamic description from ThermoCalc. It shows possible phases as a function of Al content and temperature.

Figure 2. Variety of the microstructures of the $\text{Al}_{0.3}\text{CoCrFeNi}$ CCA for different processing conditions. SEM image showing the recrystallized grains from sample **CRSA (A)** along with the $[011]_{\text{fcc}}$ zone axis diffraction pattern, and atom probe tomography (APT) showing the 3D reconstructions of Al, Co, Cr, Fe and Ni ions. The results show the presence of a single solid solution *fcc* phase.

Dark field transmission electron microscope (DFTEM) image along with the corresponding $[011]$ zone axis diffraction pattern, and atom probe tomography (APT) showing the 3D reconstructions of Al, Co, Cr, Fe and Ni ions and 15 at.% Al iso-concentration surface outlining L₁₂ precipitates in a typical APT tip from sample **CRSA620 (B)**. The compositional profile using a proximity histogram across the *fcc*-L₁₂ interface shows the compositional partitioning of various elements.

Fig. 3. Variety of the microstructures of the $\text{Al}_{0.3}\text{CoCrFeNi}$ CCA for four processing conditions. BFTEM and STEM-EDS maps of Al and Cr, and 3D reconstructions of atoms/ions Al and Cr, as marked, in a typical APT tip from samples **CR620 (C)** and **CR550 (D)**. The compositional profile using one-dimensional cylinder across the various interfaces as marked in the figure shows the compositional partitioning of various elements.

Fig. 4. (A) Mechanical behavior at room temperature of the $\text{Al}_{0.3}\text{CoCrFeNi}$ CCA. Engineering stress-strain and strain hardening vs true strain curves (inset).

(B) Ranges of ultimate tensile strength and ductility achieved by Al_{0.3}CoCrFeNi in comparison with the main classes of structural alloys including present generation automotive and aerospace engineering alloys.

(C) Materials property space for room temperature elongation vs tensile strength of steels and Al_{0.3}CoCrFeNi CCA. This strength-ductility diagram shows the range of properties achieved by Al_{0.3}CoCrFeNi CCA (represented by stars 1-4) in comparison with all steel grades which are classified in three groups in addition to stainless steels. Conventional steels include low-strength steels, e.g. interstitial-free (IF)) and mild steels, and conventional high strength steels, e.g. bake hardenable, high-strength low alloy (HSLA) and ferritic-bainitic (FB) steels. The first generation of advanced high-strength steels (AHSS) consist of ferritic matrix containing a hard martensite phase, i.e. dual phase (DP), retained austenite, i.e. transformation induced plasticity (TRIP), or small amounts of austenite and pearlite in ferrite/bainite matrix, i.e. complex phase (CP), or martensitic matrix containing small amount of ferrite/bainite, i.e. martensitic (MS) steels. The second generation of AHSS is austenitic steels with twinning induced plasticity (TWIP) and triplex steels.

Supplementary Figures

Figure S1. (A) Mechanical behavior at room temperature of the Al_{0.3}CoCrFeNi CCA. True stress-strain curves (B) **Considere's criterion for onset necking.** Work hardening rate (derivative of the true stress-strain curves) as a function of the true stress. Geometric instability is predicted to occur when the work hardening rate equals the true stress.

Figure S2. Deformation features in the single-phase Al_{0.3}CoCrFeNi HEA (CRSA). High-resolution phase-contrast image of one of the fine scale features are shown in the image on left reveals them to be nano-scale twins approximately 1nm thick (see image on the right side). The TEM of single-phase microstructure indicate that deformation occurs via combination of extensive dislocation plasticity and nano-twinning.

Figure S3. Deformation features in the triplex Al_{0.3}CoCrFeNi CCA (CR620). BFTEM recorded with $g = 200$ depicts the probable origin of the deformation twins, i.e from B2-fcc triple junction and a high angle grain boundary (HAGB). The imaging condition also revealed dense dislocations, e.g. see lower right-hand corner. These results indicate that triplex microstructure experience substantial twining compared to the single-phase fcc microstructure.

Figure S4. SEM BSED images from the different heat treatment conditions showing the drastic change in the grain sizes. The grain size in CRSA condition is 23 μm , CR-620 is 1.2 μm and in CR-550 condition is 0.4 μm .

Figure S5. Variation of toughness (approximation by calculating the area under stress-strain curve) with microstructural changes in the **Al_{0.3}CoCrFeNi CCA**

References

1. B. Cantor, I.T.H. Chang, P. Knight, A.J.B. Vincent, Mater. Sci. Eng. 375 (2004) 213-218.
2. J-W Yeh, S-K. Chen, S-J. Lin, J-Y. Gan, T-S. Chin, T-T. Shun, C-H. Tsau and S-Y. Chan, Adv. Eng. Mater. 6 (2004) 299-303.
3. B. Gludovatz, A. Hohenwarter, D. Catoor, E.H. Chang, E.P. George, R.O. Ritchie, Science. 345 (2014) 1153-1158.
4. Gwalani, Bharat, Stephane Gorsse, Deep Choudhuri, Mark Styles, Yufeng Zheng, Rajiv S. Mishra, and Rajarshi Banerjee, Acta Mater. 153 (2018) 169-185.
5. D. Miracle and O. Senkov, Acta Mater. 122 (2017) 448-511.
6. S. Gorsse, D. B. Miracle, O. N. Senkov, Acta Mater. 135 (2017) 177-187.
7. O. Bouaziz, S. Allain, C.P. Scott, P. Cugy, and D. Barbier, Current Opinion in Solid State and Materials Science. 15 (2011) 141-168.
8. Z. Li, K.G. Pradeep, Y. Deng, D. Raabe, C.C. Tasan, Nature. 534 (2016) 227-231.
9. J.Y. He, H. Wang, H.L. Huang, X.D. Xu, M.W. Chen, Y. Wu, X.J. Liu, T.G. Nieh, K. An, Z.P. Lu, Acta Mater. 102 (2016) 187.
10. Gutierrez-Urrutia, D. Raabe, Acta Mater. 60 (2012) 5791-5802.
11. Rao, J. C., H. Y. Diao, V. Ocelík, D. Vainchtein, C. Zhang, C. Kuo, Z. Tang et al. *Acta Materialia* 131 (2017) 206-220.
12. Y. Deng, C.C. Tasan, K.G. Pradeep, H. Springer, A. Kostka and D. Raabe, Acta Mater. 94 (2015) 124-133
13. Klueh, R. L., and A. T. Nelson, Journal of Nuclear Materials. 371 (2007) 37-52.
14. X.D. Xu, P. Liu, Z. Tang, A. Hirata, S.X. Song, T.G. Nieh, PK Liaw, C.T. Liu, M.W. Chen, Acta Mater. 144 (2018) 107-115

15. S. Curtze, V.-T. Kuokkala, *Acta Mater.* 58 (2010) 5129-5141.
16. Xiong, Liming, Qian Deng, Garrett J. Tucker, David L. McDowell, and Youping Chen, *International Journal of Plasticity.* 38 (2012) 86-101.
17. Byun, T. S., *Acta Materialia.* 51 (2003) 3063-3071.
18. De Cooman, B. C., Estrin, Y., & Kim, S. K., *Acta Mater.* 142 (2018) 283-362.
19. Estrin, Yu, and H. Mecking, *Acta Metallurgica.* 32 (1984) 57-70.
20. Li, DongYue, and Yong Zhang. *Intermetallics* 70 (2016) 24-28.
21. Kumar, N., M. Komarasamy, P. Nelaturu, Z. Tang, P. K. Liaw, and R. S. Mishra. *JOM* 67, (2015) 1007-1013.
22. J. Y. He, W. H. Liu, H. Wang, Y. Wu, X. J. Liu, T. G. Nieh, and Z. P. Lu, *Acta Mater.*, 62, (2014) 105–113.
23. O. Bouaziz, Y. Bréchet and J. D. Embury, *Adv. Eng. Mater.* 10 (2008) 24-36.
24. B. Chéhab, H. Zurob, D. Embury, O. Bouaziz and Y. Brechet, *Adv. Eng. Mater.* 11 (2009) 992-999.
25. D. Embury and O. Bouaziz, *Annu. Rev. Mater. Res.* 40 (2010) 213–241.
26. Basu, Indranil, Václav Ocelík, and Jeff Th M. De Hosson. *Acta Materialia* 150 (2018) 104-116.
27. Basu, Indranil, Václav Ocelík, and Jeff ThM De Hosson. *Acta Materialia* 157 (2018) 83-95.
28. Basu, Indranil, Václav Ocelík, and Jeff Th M. De Hosson. *Journal of Materials Research* 1-22.

